Monthly Notices
of the
ROYAL ASTRONOMICAL SOCIETY

MNRAS **464,** 3281–3296 (2017)
Advance Access publication 2016 October 8

doi:10.1093/mnras/stw2570

Optical, UV, and X-ray evidence for a 7-yr stellar cycle in Proxima Centauri

B. J. Wargelin,[1]★ S. H. Saar,[1] G. Pojmański,[2] J. J. Drake[1] and V. L. Kashyap[1]

[1]*Harvard-Smithsonian Center for Astrophysics, 60 Garden Street, MS-70, Cambridge, MA 02138, USA*
[2]*Astronomical Observatory University of Warsaw, Al. Ujazdowskie 4, PL-00-478 Warszawa, Poland*

Accepted 2016 October 5. Received 2016 October 1; in original form 2016 July 1; Editorial Decision 2016 October 3

ABSTRACT

Stars of stellar type later than about M3.5 are believed to be fully convective and therefore unable to support magnetic dynamos like the one that produces the 11-yr solar cycle. Because of their intrinsic faintness, very few late M stars have undergone long-term monitoring to test this prediction, which is critical to our understanding of magnetic field generation in such stars. Magnetic activity is also of interest as the driver of UV and X-ray radiation, as well as energetic particles and stellar winds, that affects the atmospheres of close-in planets that lie within habitable zones, such as the recently discovered Proxima b. We report here on several years of optical, UV, and X-ray observations of Proxima Centauri (GJ 551; dM5.5e): 15 yr of All Sky Automated Survey photometry in the *V* band (1085 nights) and 3 yr in the *I* band (196 nights), 4 yr of *Swift* X-Ray Telescope and UV/Optical Telescope observations (more than 120 exposures), and nine sets of X-ray observations from other X-ray missions (*ASCA*, *XMM–Newton*, and three *Chandra* instruments) spanning 22 yr. We confirm previous reports of an 83-d rotational period and find strong evidence for a 7-yr stellar cycle, along with indications of differential rotation at about the solar level. X-ray/UV intensity is anticorrelated with optical *V*-band brightness for both rotational and cyclical variations. From comparison with other stars observed to have X-ray cycles, we deduce a simple empirical relationship between X-ray cyclic modulation and Rossby number, and we also present *Swift* UV grism spectra covering 2300–6000 Å.

Key words: stars: activity – stars: individual: (Proxima Cen) – stars: late-type – stars: rotation.

1 INTRODUCTION

Stellar activity cycles, seen in the Sun and many late-type stars, are driven by magnetic activity and therefore reflect a star's magnetic field strength, internal structure, rotation, and evolution. Studying those cycles can provide key information on the dynamo process, which powers magnetic regeneration in stars, accretion discs, and planets. Many details of that process, however, remain poorly understood, even for the 11-yr solar cycle. Observational comparisons with other stars are therefore vital for constraining models of magnetic activity and explaining the presence or lack of stellar cycles.

Understanding stellar magnetic activity is also relevant to studies of exoplanets because starspots and flares can mimic or obscure the signatures of planets (Queloz et al. 2001) and may affect those planets' habitability. This latter subject is especially interesting in light of the recent discovery of an exoplanet orbiting in the habitable zone of our Sun's nearest neighbour, Proxima Centauri. Proxima b has a minimum mass of about 1.3 times that of the Earth and an orbital period of 11.2 d with a semimajor axis of only 0.049 au, about one-eighth Mercury's orbital radius (Anglada-Escudé et al. 2016). A key factor in planetary habitability is the effect on the atmosphere of X-ray/UV radiation and the stellar wind (e.g. Lammer et al. 2003; Khodachenko et al. 2007; Penz & Micela 2008; Cohen et al. 2015; Owen & Mohanty 2016, and references therein) which are ultimately driven by the stellar magnetic field.

Cycles in most cool stars (F–M) are thought to arise from the interplay of large-scale shear [differential rotation (DR)] and small-scale helicity in an $\alpha\Omega$ dynamo. The current paradigm has the Ω effect sited in the tachocline layer at the bottom of the convection zone (Dikpati & Charbonneau 1999). Stars later than type ∼M3.5 are expected to be fully convective (Chabrier & Baraffe 1997) with their magnetic activity probably arising from the α^2 process, which is not considered conducive to generating cyclic behaviour, although some modellers suggest that cycles may be possible in certain parameter regimes (e.g. Rüdiger, Elstner & Ossendrijver 2003; Gastine, Duarte & Wicht 2012; Käpylä, Mantere & Brandenburg 2013). Evidence has also recently emerged that fully convective stars share the same rotation–activity relation as stars

★E-mail: bwargelin@cfa.harvard.edu

with radiative cores, supporting the idea that the tachocline is not a key ingredient of solar-type dynamos (Wright & Drake 2016). Proof of the existence of cycles in fully convective stars and how their character varies with stellar properties would greatly advance our understanding of stellar dynamos but such stars' intrinsic faintness, often coupled with short-term variability that can mask longer term trends, makes this difficult.

The longest running program to look for signs of cyclic magnetic activity is the HK Project at Mount Wilson Observatory (MWO), which began c. 1966 (Wilson 1978; Baliunas et al. 1995) and monitors chromospheric Ca II H and K lines (3969 and 3934 Å) as indicators of the strength and covering fraction of stellar magnetic fields. This project currently includes about 300 stars of spectral type F–K, but only a single M star (HD 95735; Lalande 21185; dM2) because of the general faintness of M dwarfs and the relative weakness of their Ca II lines.

Other monitoring projects, including the High Accuracy Radial Velocity Planet Searcher (HARPS; Mayor et al. 2003), the McDonald Observatory (MDO) M Dwarf Planet Search (Cochran & Hatzes 1993; Endl et al. 2003), the Complejo Astronómico El Leoncito (CASLEO)/HKα Project (Cincunegui & Mauas 2004), the REsearch Consortium On Nearby Stars (RECONS; Henry, Kirkpatrick & Simons 1994; Hosey et al. 2015), and the All Sky Automated Survey (ASAS; Pojmański 1997, 2002) have increased the number of M dwarfs under study, employing a variety of stellar activity metrics. These newer programs have now been running for over a decade and several papers on their early results for M stars have been published in the past few years.

Using HARPS spectral data collected over periods as long as 7 yr, Gomes da Silva et al. (2011, 2012) studied 28 M0–M3.5 stars along with Barnard's Star (M4) and Proxima Cen (M5.5). Roughly one third of the stars, but not Barnard's Star or Prox Cen, showed long-term variability in at least two of the optical lines studied (Ca II, H α, He I D3, Na I D). (Note that the Prox Cen observations, collected during roughly 40 nights over 6 yr, had the lowest signal-to-noise ratio of the ∼30 stars studied.) Anglada-Escudé et al. (2016) used those and newer HARPS data, along with spectral and photometric data from other instruments, in their study of Prox Cen and also did not see a cycle, although they did note roughly 80-d rotational periodicity.

Robertson et al. (2013) analysed H α intensities in ∼90 M0–M5 stars specifically chosen for their inactivity (indicated by a lack of *ROSAT* soft X-ray detections) in the MDO program, including a dozen M4's and a few M5's. At least seven stars showed periodicity, the latest types being M4 for GJ 476 (but listed as type M2.5 in SIMBAD) and M5 for GJ 581, which Gomes da Silva et al. (2012) also found to be periodic but listed as type M2.5. GJ 581 was also studied, along with 263 other M2–M8 stars in the RECONS program, using *VRI* photometry by Hosey et al. (2015) who did *not* see a cycle. They did, however, find four other stars with multiyear periodic behaviour indicative of a cycle, but three of those systems were binaries and the other cycle was only tentative. Vida, Kriskovics & Oláh (2013) studied four systems (one K3, one M4, and the others ∼M1) with very short rotation periods (∼0.45 d) and found similarly short cycles ranging from 0.84 to 1.45 yr in all except the M4. Other nearly fully convective stars showing signs of a cycle include AD Leo (M3; Buccino et al. 2014), GJ375 (M3; Díaz et al. 2007), and perhaps EV Lac (M3.5; Alekseev 2005).

The paucity of results for late-type M stars is not due to lack of interest but because of these stars' faintness and the difficulty of finding suitable activity metrics. Of the handful of stars with stellar type M4 or later noted above, the aptly named Proxima Cen (dM5.5; Bessell 1991) is by far the closest (1.305 pc; Lurie et al. 2014) and easiest to observe and several authors have reported indications that it may have a cycle. Benedict et al. (1998), analysing 5 yr of photometry data from the *Hubble* Fine Guidance Sensors, suggested a 3.0-yr cycle, though with low confidence. Cincunegui, Díaz & Mauas (2007), measuring the H α line-to-continuum on 24 nights over 7 yr and excluding obvious flares, made Lomb–Scargle periodograms and found a 1.2-yr period with peak-to-peak amplitude variations of 25 per cent but a false alarm probability of 35 per cent. Lastly, Endl & Kürster (2008) found an 'intriguing peak' in 76 nights of radial velocity measurements, but the period of that peak roughly matches the 7-yr span (2000–2007) of their observing program, and they did not see evidence for an 83-d rotation period (see below).

The most compelling optical evidence for a stellar cycle in Prox Cen comes from the ASAS project (Pojmański 2002), which monitors millions of stars brighter than ∼14th magnitude in the *V* and *I* bands in the southern (beginning 1997) and northern (since 2006) skies. Currently, *V*-band data from the third of four data collection phases (ASAS-3; 2000–2010) are available online, along with *I*-band data from ASAS-2 (1998–2000, not including Prox Cen). Using 5 yr of *V*-band data from ASAS-3 supplemented with UV data from the *IUE* and *FUSE* missions, Jason et al. (2007) saw indications of a 'probable' cycle of 6.9 ± 0.5 yr in Prox Cen, later revised to 7.6 yr in a *Chandra* observing proposal by Guinan (2010). Savanov (2012) later calculated amplitude power spectra using 9 yr of ASAS data and also saw a broad peak around 8 yr, along with several other peaks at shorter periods. [We learned shortly before acceptance of this paper that Suárez Mascareño et al. (2016) also analysed ASAS-3 data and found cycles in seven and perhaps as many as nine stars of type M4 or later, including Prox Cen with $P_{\rm rot}$ = 6.8 ± 0.3 yr.]

An activity cycle in a fully convective M star like Prox Cen would be exciting if confirmed, as it would provide evidence that (1) another type of $\alpha\Omega$ dynamo must exist, such as one driven by shear within the convective zone in the absence of a tachocline, as suggested in recent models by Brown et al. (2011a,b); (2) there is a magnetically stabilized layer deep in cool M dwarfs that can act like a tachocline for flux storage/amplification (e.g. Mullan & MacDonald 2001); or (3) α^2 dynamos can indeed support cycles, as suggested by some work including Rüdiger et al. (2003) and Chabrier & Küker (2006).

Whether or not Prox Cen has a stellar cycle, a vital parameter in understanding its magnetic activity is its rotation rate. Guinan & Morgan (1996) used *IUE* Mg II intensities (∼2800 Å) from twice-weekly observations over ∼4 months in 1995 to deduce a rotation period of 31.5 ± 1.5 d with 20–25 per cent variations, later revised to 30.5 ± 1.5 (Jay et al. 1997), both reported in conference presentations. The previously mentioned work by Benedict et al. (1998) using *Hubble* Fine Guidance Sensor (FGS) data derived a rotation period of 83.5 d with 6.6 per cent (0.069 mag) peak-to-peak amplitude consistent with rotational modulation caused by a single large starspot. [Smaller variations at half that period were sometimes seen and ascribed to two starspots ∼180° apart. Earlier work by Benedict et al. (1993) using a shorter span of FGS data also found a period of 42 d.] More recently, Kiraga & Stepień (2007), Savanov (2012), and Suárez Mascareño, Rebolo & González Hernández (2016), using between 5 and 9 yr of ASAS data, all derived periods of 83 d. Reiners & Basri (2008) comment that this period is longer than expected given Prox Cen's activity level and the magnetic field strength of ∼600 G that they inferred from Zeeman broadening in high-resolution spectra.

1.1 X-ray period monitoring

As noted above, M stars are in general quite faint in the optical band, and any variations in Prox Cen's optical emission caused by magnetic activity cycles are likely to be at the few per cent level. UV/X-ray emission, however, is a much more sensitive indicator of magnetic activity in late-type stars, particularly M dwarfs. In the Geostationary Operational Environmental Satellite 1–8 Å (1.5–12 keV) band used to monitor solar emission, the quiescent X-ray flux (L_X) varies by two or three orders of magnitude over a cycle (Wagner 1988; Aschwanden 1994), depending on how stringently flares are filtered out. Judge, Solomon & Ayres (2003) estimate that in the softer *ROSAT* band (0.1–2 keV) the Sun's L_X varies by a factor of ∼6 over a cycle, while optical-band amplitudes are of order 0.1 per cent.

A major challenge with X-ray monitoring, however, is maintaining a sustained campaign by a single mission. Long gaps in temporal coverage hamper periodicity analyses, and instrumental responses can differ a great deal from one telescope to another, making comparisons problematic. An example is provided by α Cen (G2V+K1V). Ayres et al. (2008) reported that an apparent rapid decrease in X-ray emission from α Cen A was greatly exaggerated by energy-dependent differences among the multiple satellite/instrument configurations used to observe it. Ayres (2009) followed that paper with a painstaking analysis that combined 13 yr of X-ray data from three missions and five instruments, and derived a tentative cycle in α Cen B of 9 yr, in agreement with an estimate of 8.36 yr derived from Mg II and Ca II emission by Buccino & Mauas (2008) and an 8.8-yr period found by DeWarf, Datin & Guinan (2010). A follow-on paper (Ayres 2014) that included nine more twice-yearly *Chandra* High Resolution Camera for Imaging (HRC-I) observations refined the X-ray period to 8.1 ± 0.2 yr with a factor of 4.5 intensity variation and also suggested that α Cen A may have a ∼19-yr cycle.

Three other late-type stars have also been reported to have X-ray cycles. Hempelmann et al. (2006) studied X-ray data on 61 Cygni A (K5V) from *ROSAT* (eight measurements over 1993–1997) and *XMM–Newton* (eight over 2002–2005) and observed X-ray fluxes vary by more than a factor of two over a 7.3-yr cycle, in agreement with 40 yr of Ca II measurements. The latest update (Robrade, Schmitt & Favata 2012) reports the same cycle period with factor-of-three intensity variations over 10 yr of twice-yearly *XMM–Newton* observations. (*XMM–Newton* is also monitoring α Cen but the A and B components are not well resolved.)

The next X-ray cycle measurement is by Favata et al. (2008), who used twice-yearly *XMM–Newton* observations of HD 81809 (G2+G9) covering 2001–2007 to reveal a well-defined cycle (presumed to be the G2) with quiescent L_X varying by a factor of 5 or 6 and matching the 8.2-yr period seen in Ca II HK lines. Lastly, Sanz-Forcada, Stelzer & Metcalfe (2013) reported the X-ray detection of a somewhat irregular 1.6-yr activity cycle in the young solar-type star ι Hor that had previously been discovered using Ca II HK emission (Metcalfe et al. 2010). X-ray intensity varied by about a factor of two over the 14 *XMM–Newton* observations that spanned 21 months in 2011–2013. Although not all stars will exhibit X-ray cycles (e.g. Hoffman, Günther & Wright 2012; Drake et al. 2014), the above examples illustrate the potential of detecting cycles using X-ray monitoring. Prox Cen is however, a more challenging case because it flares more often and its X-ray cycle amplitude appears to be smaller than for these other stars.

In Section 2 we analyse 15 yr of ASAS optical data, followed by analysis of 4 yr of *Swift* data in Section 3, and then interpretation of the optical, UV, and X-ray results in Section 4. Section 5 examines *Swift* observations in concert with data from other X-ray missions in order to extend the period of high-energy monitoring, followed by a summary of results in Section 6.

2 OPTICAL DATA

As noted in Section 1, Kiraga & Stepień (2007), Savanov (2012), and Suárez Mascareño et al. (2016) measured rotation periods of around 83 d using ASAS-3 data, in good agreement with the 83.5-d period measured by Benedict et al. (1998) using *Hubble* data. Guinan (2010) cites a period of 83.7 d and an activity cycle of ∼7.6 yr derived from an unpublished analysis of ASAS data, and also says that *ROSAT*, *XMM–Newton*, and *Chandra* data show a 'corresponding coronal X-ray cycle with an expected minimum during 2010/2011.'[1] Using the same ASAS data, Suárez Mascareño et al. (2016) measured a cycle of 6.8 ± 0.3 yr.

For our analysis, we downloaded the complete set of ASAS-3 (Pojmański 2002) *V*-band data on Prox Cen covering 2000 December 27 to 2009 September 11 from http://www.astrouw.edu.pl/asas/, and also added manually processed data from the ASAS-4 program covering 2010 July 08 to 2015 August 16. We used a 4-pixel (1 arcmin) aperture (the middle of five available, producing the MAG_2 measurements) for photometry as this provided the lowest overall uncertainties. Of the 1462 measurements with A or B quality flags, we kept only those with magnitudes that fell within three standard deviations of the mean (grouped by observing season, which approximately coincides with calendar year). The remaining 1433 observations, typically 3 min long, were made on 1085 nights. Calibration of the ASAS-4 system, particularly vignetting and point spread function (PSF), is not complete, so we used 33 stars to normalize the ASAS-4 measurements to ASAS-3, with an estimated uncertainty of around 0.02 or 0.03 mag. Note that since ASAS magnitudes are based on the Tycho-2 system (V_T, B_T) and no colour terms were included in ASAS transformation of instrumental data, they can differ slightly from the standard Johnson system, particularly for red stars; Prox Cen's *V* magnitude is typically given as around 11.13 (e.g. Jao et al. 2014).

We also studied ASAS-3 *I*-band data, which were less extensive than for the *V* band, covering only the 2003, 2005, and 2006 seasons. There were 249 measurements on 196 nights with A or B quality, of which roughly half were collected on the same nights as *V*-band observations. We used the MAG_3 measurements (5-pixel aperture), which had the smallest scatter.

Our search for a rotation period and stellar cycle uses a Lomb–Scargle (L–S) floating mean periodogram analysis (Scargle 1982) with the implicit assumption that emission nonuniformities such as starspots persist for multiple rotation periods and modulate the observed quiescent emission. In the *V*-band data, we find two extremely strong peaks of $P = 83.1 \pm 0.05$ and 2576 ± 52 d (7.05 ± 0.15 yr; errors following Baliunas et al. 1995) that we interpret as the mean rotational and magnetic cycle periods, respectively (see Fig. 1). Results when analysing the ASAS-3 data alone were 82.9 d and 7.91 yr. Collectively changing the ASAS-4 measurements by up to ±0.05 mag to gauge the effect of cross-calibration uncertainties barely changed the periods. For both period determinations, the standard L–S False Alarm Probability (FAP) $\ll 10^{-20}$ (Horne & Baliunas 1986) although there are many reasons for believing these L–S FAPs overestimate the certainty of the detections (e.g. Baliunas

[1] As explained in Section 3.3, we find an X-ray maximum around that time.

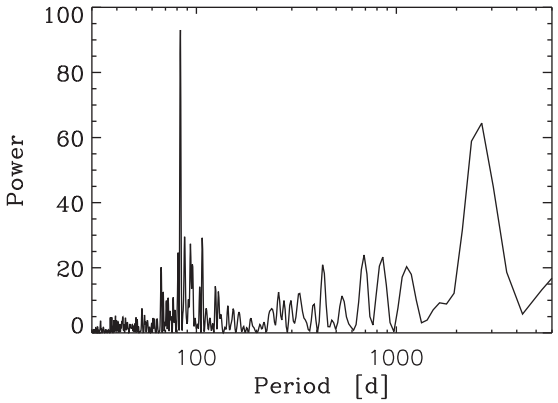

Figure 1. Lomb–Scargle periodogram of *V*-band ASAS data. Rotation peak is at 83.1 d and the broad peak around 2600 d (∼7 yr) is from the stellar cycle.

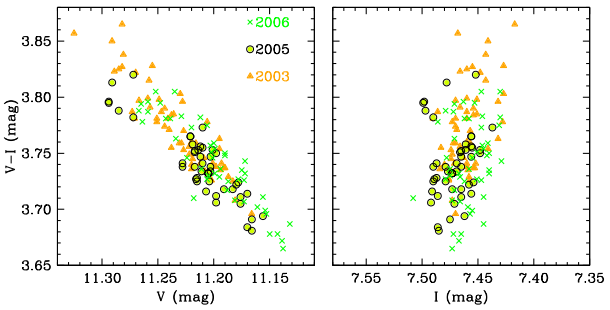

Figure 2. Colour diagrams illustrating changes in *V* over time, while *I* remains nearly constant.

et al. 1995). Monte Carlo simulations for randomly reordered data with the same time spacing yield FAPs $\sim 1 \times 10^{-6}$, so the periods are robust.

The smaller set of *I*-band data yielded a lower confidence rotation period of 82.7 d but spanned too little time to say anything about a multiyear cycle. *V–I* colours show a clear trend with *V* (Fig. 2) such that as the star gets brighter it also becomes less red, suggesting that cool starspots are driving the variation. The lack of a clear *V–I* trend with *I* suggests that both spots and the quiet photosphere are contributing significantly to emission in this band, again underlining that variation is due to cool features, which are more visible in the red.

To determine the amplitudes of the *V*-band modulations, we first fitted and subtracted the 7.05-yr cyclic modulation (peak-to-peak 0.040 mag = 3.8 per cent) and then fitted another sinusoid to the residuals to find the rotational amplitude (peak-to-peak 0.042 mag = 3.9 per cent). Fig. 3 (top panel) plots the data along with the 7-yr cycle found by the L–S analysis. To better show the cyclic behaviour, we also plot yearly averages with error bars. (Some of the later years had relatively few measurements and were grouped together.) In the bottom panels, we separate the data by year, subtract the 7-yr modulation, and phase all the data using a common 83.1-d period.

Data are colour coded to roughly indicate various phases of the 7-yr cycle (red for minimum, orange for rising, etc.) but there is no obvious correlation of rotational phasing or amplitude with cycle phase. The 2010–2012 group has a very well defined modulation (see the inset in the top panel) with a period of 86.3 d. With the period fixed at 83.1 d, rotational phasing remains remarkably constant ($\Delta\phi$

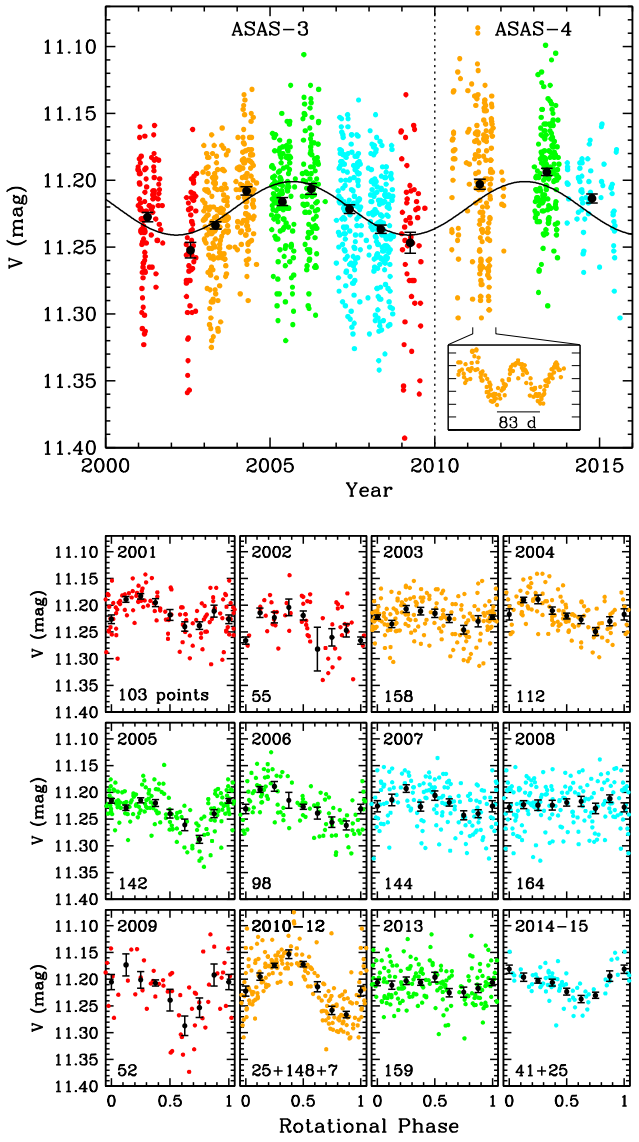

Figure 3. Top: ASAS *V*-band data with grouped averages (black) and best-fitting 7.05-yr cycle (sinusoid). Inset uses same vertical scale. Bottom: Data are separated by observing season and phased to a rotation period of 83.1 d, with 7.05-yr cycle modulation subtracted. Some years have few measurements and are grouped with other years. Colours correspond to associated time intervals in the top panel; black points with error bars are averages over 1/8-period bins.

between −0.08 and +0.15) over nearly the entire 15 yr of coverage, despite significant changes in the modulation amplitude, which falls to essentially zero in 2008 before recovering. The apparently stable phasing is consistent with the findings of Berdyugina (2007) that persistently active longitudes are common in active stars.

If, instead of adopting a fixed average $P_{\rm rot}$, we perform a period analysis of each time group, we find some evidence for DR. Including the 2010–2012 group noted above with its 86.3-d period, six intervals have FAP $\leq 10^{-3}$, ranging from $P_{\rm rot} = 77.1$ d (2001 season; FAP $= 8.4\times 10^{-6}$) to $P_{\rm rot} = 90.1$ d (2009; FAP $= 7.0\times 10^{-4}$; these latter data exhibit modulation with a period of 45 d that we interpret as arising from nonuniformity on roughly opposite sides of the star). This yields a fractional DR estimate of $\Delta P_{\rm rot}/\langle P_{\rm rot}\rangle \geq 0.16$, similar to the Sun. Note that this is a lower limit to DR since we are likely not sampling all latitudes on Prox Cen. Another

common DR measure uses the spread of observed periods: $N\sigma_P/\langle P_{\rm rot}\rangle$. For $N = 3$ (e.g. Lehtinen et al. 2016), this measure gives an identical result.

We believe this is the first DR measurement on such a slowly rotating, fully convective star. The estimated $\Delta P_{\rm rot}$ implies $\Delta\Omega/\Delta\Omega_\odot = 0.33$, which puts Prox Cen at the edge of the observed $\Delta\Omega - Ro^{-1}$ distribution for single dwarfs (a factor of ∼3 below than the overall trend; see Saar 2011, their fig. 2 left). The measured DR is in better agreement with the $\Delta\Omega - \Omega$ relation (∼40 per cent above the trend's extrapolation to lower Ω; Saar 2011, their fig. 2 right). We do not observe any correlation between $P_{\rm rot}$ and cycle phase.

Interestingly, although Hosey et al. (2015) included Prox Cen in their RECONS study of M stars, obtaining 35 nights of data from 2000 to 2013 and measuring a standard deviation of 0.0285 mag (2.7 per cent) (the 12th largest variability among the 114 stars with *V* photometry in their data set), they did not note any cyclic behaviour. For comparison, the ASAS *V*-band data exhibit a standard deviation of 0.0426 mag (4.0 per cent) while the Sun's optical intensity varies by ∼0.1 per cent over its cycle. One possibility is that the much sparser RECONS monitoring occurred mostly when Prox Cen was near its mean brightness, which would also explain why their standard deviation is smaller than ours. In any case, the 15 yr of ASAS observations display highly significant sinusoidal variations consistent with a 7-yr stellar cycle. Further interpretation of those results is aided by analysis of *Swift* X-ray and UV data, which we now discuss.

3 *Swift* OBSERVATIONS

The *Swift* satellite is primarily designed to detect and study gamma-ray bursts (GRBs) using its Burst Alert Telescope but also carries an X-Ray Telescope (XRT; Burrows et al. 2005) and UV/Optical Telescope (UVOT; Roming et al. 2005) to more accurately determine source positions and provide wider spectral coverage. Roughly 20 per cent of the total observing time is available to observe non-GRB Targets of Opportunity (TOOs) and other sources approved in advance through the Guest Investigator (GI) program.

From 2009 April through 2013 February (*Swift* Cycles 5–8), using a mix of GI time and TOO time generously provided by the *Swift* PI, Neil Gehrels, we obtained 45 XRT and/or UVOT observations of Prox Cen divided into 125 separate exposures or 'snapshots.' *Swift* operates in low Earth orbit (∼95-min period) and snapshots rarely exceed 2000 s, with typical exposures of several hundred seconds. The XRT was operated in Photon Counting event mode (time-tagged events), and data were collected approximately simultaneously with UVOT data.

The first eight observations (21 snapshots; see Table 1) used the UVOT UV grism (Kuin et al. 2015) in imaging mode, covering roughly 1700–5000 Å in first order. Resolving power is ∼75 at 2600 Å, and effective area (EA) peaks near the Mg II HK blend (2803.5 + 2796.3 Å), which is an analogue of the optical Ca II HK doublet but brighter in M stars. Most of the grism snapshots were bracketed by short imaging-mode exposures using the UVW1 and/or UVW2 filters which have bandpasses of ∼1000 Å centred near 2500 and 1900 Å, respectively.

As discussed in Section 3.1, source crowding in the UVOT field (Fig. 5) can lead to overlapping grism spectra and was a significant problem in Prox Cen's field, which lies roughly towards the Galactic Centre (l, b = 313.925, −1.917). The accompanying short filter exposures did not suffer this problem so after the first eight grism observations we ran subsequent UVOT exposures solely using the UVW1 filter in event mode.

Table 1. *Swift* observations.

ObsID	Snapshots	Date	Exposure times (s)		
			XRT	UVW1	Grism
90215002	502ab	2009 April 23	0.0	158.0	833.8
90215003	503ab	2009 May 10	769.7	153.1	294.9
90215005	505a[a]bc	2009 May 13	3111.5	308.3	1084.8
90215006	506ab	2009 May 27	2680.3	222.0	1133.8
90215007	507abc[a]d	2009 June 19	2590.0	222.5	733.8
90215008	508abc	2009 July 10	1827.8	155.8	534.8
90215009	509abc	2009 August 01	1812.7	150.9	434.8
90215010	510ab	2009 August 22	2019.9	167.8	834.8
90215011	511ab	2009 September 09	2146.3	2174.8	–
90215012	512abc	2009 October 03	1840.2	1873.5	–
90215013	513abcde	2009 October 23	2538.4	2570.9	–
90215014	514abc	2009 December 14	2146.2	2163.8	–
90215015	515abc	2009 December 30	2232.0	2322.4	–
90215016	516ab	2010 January 19	0.0	2025.1	–
90215017	517a	2010 January 20	1846.0	1857.9	–
90215018	518abc	2010 February 04	2030.9	0.0	–
90215019	519abcde	2010 February 08	2366.9	2421.8	–
90215020	520abc	2010 March 04	1847.8	1872.0	–
90215021	521ab	2010 March 24	1864.8	1883.9	–
90215022	522ab	2010 April 09	2978.8	3005.5	–
31676001	601abc	2010 July 10	1892.1	1893.6	–
31676002	602abcd[a]	2010 December 07	2894.2	2994.9	–
31676003	603ab	2011 March 12	3260.5	3263.6	–
31676004	704abcd	2011 September 04	1989.8	1987.1	–
31676005	705abc	2011 September 08	776.2	740.4	–
31676006	806ab	2012 March 30	1953.2	1970.8	–
31676007	807ab	2012 April 02	2434.5	2443.5	–
31676008	808abc	2012 April 06	2304.3	2322.2	–
31676009	809ab	2012 April 10	2557.5	2563.0	–
31676010	810abcde	2012 April 14	1394.1	1396.7	–
91488001	890abc	2012 April 18	2850.8	2867.9	–
31676011	811abcd	2012 April 22	1027.9	1032.8	–
31676012	812ab	2012 April 26	1980.8	1992.8	–
31676013	813ab	2012 April 30	2504.8	2524.7	–
31676014	814abc	2012 May 04	2534.9	2545.8	–
31676015	815ab	2012 May 12	804.9	814.0	–
31676016	816a	2012 May 13	847.5	860.2	–
31676017	817abcde	2012 May 16	2389.5	2396.7	–
31676018	818ab	2012 May 24	2103.6	2115.3	–
31676019	819ab	2012 May 28	2214.0	2220.2	–
31676020	820abcde	2012 July 03	1000.4	1009.0	–
31676021	821a	2012 June 12	687.0	704.4	–
31676022	822abc	2012 June 16	2128.7	2134.2	–
91488002	892a[a]bc	2012 September 18	3053.9	3020.4	–
91488003	893ab	2013 February 18	2697.8	2698.7	–

Notes. – Snapshot labels use the leading digit to denote the *Swift* observing Cycle, the next two digits for the observation number within that Cycle, and abc... to indicate the snapshots within each observation.
[a]Snapshot was split into pre-flare and flaring portions.

As seen in Table 1, our observations were concentrated in two time periods. About 20 observations with an average spacing of ∼18 d were made in Cycle 5, and 18 observations in Cycle 8 with average 10-d spacing. The Cycle 5 observations were primarily designed to look for signs of the 1.2-yr periodicity suggested by Cincunegui et al. (2007), and the second group focused on finding rotational variations with periods of several weeks. Several other observations were spaced more widely through Cycles 6, 7, and 8 to support multiyear monitoring. Total exposures for each Cycle were respectively 38.7 (25.7 for UVW1), 6.2, 2.7, and 39.5 ks.

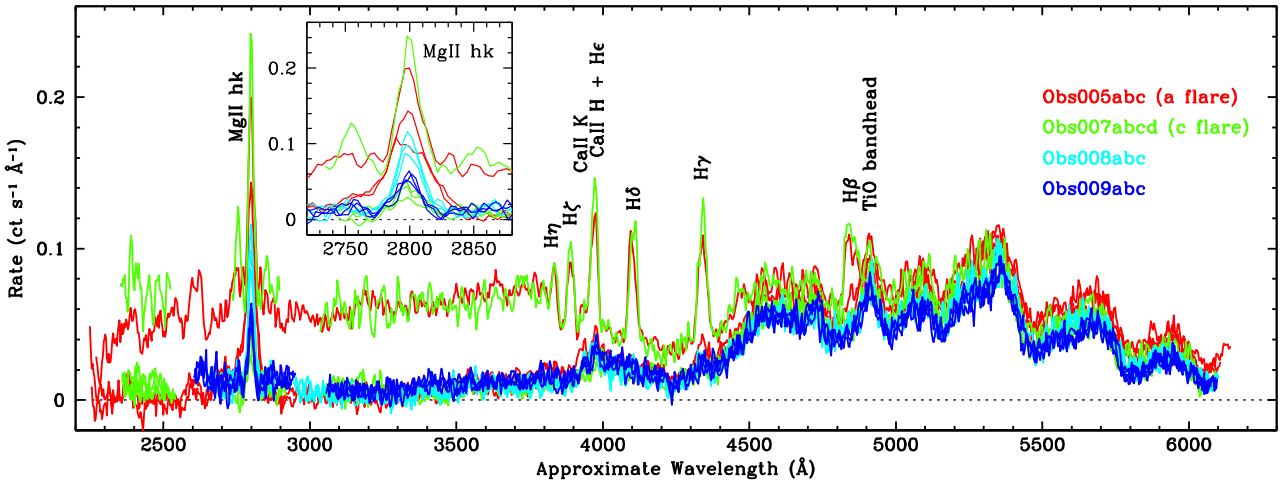

Figure 4. Background-subtracted UV grism spectra with approximate wavelength calibration and detail of Mg II emission. The two higher rate spectra were obtained during strong flares. Portions of some spectra are excluded because of contamination from other sources. Pure first-order emission extends to ∼2700 Å. Beyond this, higher orders become increasingly important and may dominate beyond ∼5000 Å. Wavelengths also become more uncertain but the pronounced broad features beyond H β are mostly due to TiO bandheads.

3.1 Grism spectra

The design and calibration of both UVOT grisms are thoroughly described by Kuin et al. (2015). We used the UV grism in 'clocked' mode to restrict the UVOT field of view and block some of the field stars and their associated spectra. As mentioned above, our hope was to use the Mg II HK line-to-continuum ratio as a stellar activity metric but even in clocked mode, spectra from other stars often overlapped part or all of the Prox Cen spectrum. As a result, we used the grism for only eight observations before switching to the UVW1 filter. Only four of the grism observations provided clean Mg II HK lines, and only about half of those had uncontaminated adjoining continuum. Given this limited data set, we did not expend the considerable effort required to create spectra with fully calibrated intensities and wavelengths.

We did, however, extract spectra using the `uvotimgrism`[2] tool, adjusted the spectral and background regions to minimize interference from other stars, and then manually interpolated across contaminated portions of the background and applied approximate wavelength corrections based on known spectral features. Results for the four observations (13 snapshots) with clean Mg II HK lines are shown in Fig. 4, excluding contaminated regions of each spectrum. Apart from the prominent Mg II HK blend which varies significantly from one observation to another (see figure inset), the quiescent spectra are nearly identical. Note that the Ca II HK and hydrogen Balmer series lines commonly seen in K, G, and F stars are weak or absent in this M star, except during strong flares (Obs505a and Obs507c) when the continuum is also enhanced, thus illustrating why S/N was so low for the HARPS study of Prox Cen (Gomes da Silva et al. 2011, 2012), which measured the Ca II HK, He I D3 (5876 Å), Na I D1 (5890+5896 Å), and H α (6562 Å) lines.

3.2 XRT and UVOT data extraction

The XRT focuses X-rays on to a 600 × 600-pixel CCD (2.36 arcsec pixels) with a half-power diameter of 18 arcsec. Prox Cen has a large proper motion of 3.85 arcsec per year so the expected source position

[2] http://heasarc.gsfc.nasa.gov/docs/software/ftools

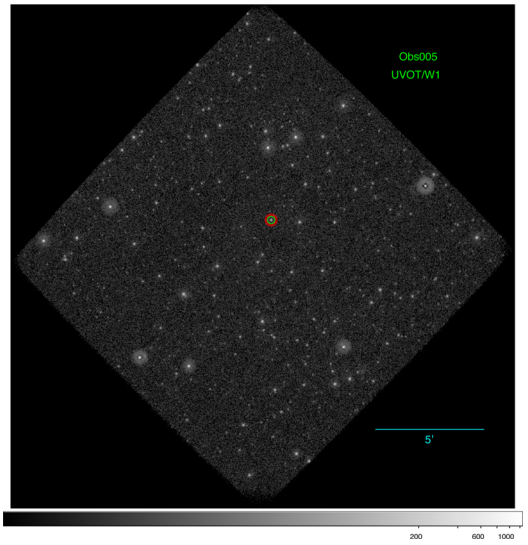

Figure 5. Example UVOT image with UVW1 filter. Source and background counts were extracted from the green circle and red annulus, respectively.

was calculated for each observation in order to centre the extraction region. From examining a higher resolution *Chandra* observation (ObsID 49899), we determined that nearby sources unresolved by *Swift* contribute no more than 1 per cent of the counts in our 40-pixel-radius (94 arcsec) source region. Point source emission within the 25-times larger background region, an annulus with radii of 60 and 209 pixels, is similarly unimportant. All our XRT observations used Photon Counting mode, which has a time resolution of 2.5 s. Event pile-up is negligible for Prox Cen except during major flares.

In contrast, the UVOT field is very crowded and some care is needed in selecting the source and background regions (see Fig. 5). Spatial resolution is ∼2.5 arcsec with 0.502 arcsec pixels. As noted earlier, the grism observations were made in imaging mode while subsequent observations using the UVW1 filter were made in event mode, with 0.11 ms time resolution. We used circular source extraction regions with 10-pixel radii and annuli of the same area (radii 13.0–16.4 pixels) for the background.

There are 45 observations in total, two of them without XRT data and one missing UVOT data, divided into 125 snapshots averaging ∼720 s each. After examining light curves, four of the snapshots were split into pre-flaring and flaring sections, as noted in Table 1. Background-subtracted rates for each snapshot were easily calculated for the UVOT data[3] but the XRT analysis was more complicated. First, XRT data were divided by energy into a Soft band (0.2–1.2 keV) and a Hard band (1.2–2.4 keV) with the rationale that the harder band, although containing fewer counts, is more sensitive to variations in stellar activity. The XRT CCD also suffered micrometeoroid damage early in the mission, leaving some columns and pixels inoperative. The XRT PSF is broad enough, however, that corrected event rates can be estimated even when part of the source falls on the damaged regions by using the 'Swift-XRT data products generator'[4] (Evans et al. 2009) which also applies corrections for event pile-up (only significant during flares).

3.3 Periodicity analysis

3.3.1 Selection of quiescent rates

As noted above, flaring tends to obscure underlying longer term trends in emission, particularly in the X-ray band where flares can reach intensities tens or even hundreds of times the quiescent level. Unlike the G and K stars described in Section 1.1, Prox Cen is a relatively active star and determining when emission is quiescent or flaring is challenging with limited temporal coverage. *Swift* snapshots are typically only several hundred seconds long, too short to tell whether the observed emission is quiescent or flaring. Each of our observations, however, comprises one to five snapshots spaced at intervals of one or more *Swift* orbits (∼95 min), relatively long compared to typical flare time-scales of a few hundred or thousand seconds, making it much more likely to sample and reliably identify quiescent periods during a given observation. This effort is also aided by having data in three somewhat independent wavebands: UVW1, and Soft and Hard X-rays.

Although multiple wavebands and convenient snapshot spacing help, there is still the fundamental problem of limited exposure time and event rates, and determining 'the' quiescent emission level in each band during an observation remains a challenge. After trying several approaches, including measuring X-ray hardness ratios and various statistical methods, we chose a method that, roughly speaking, uses the lowest rate snapshot within each observation.[5] This was simple for the 19 observations in which the lowest rate snapshot was the same in all three wavebands. In 18 other cases, there was no common lowest rate snapshot and we chose the one with the highest significance 'lowness,' sometimes averaging rates from two or even three snapshots if they were very short and/or their error bars substantially overlapped. In four observations, emission is decreasing from a prior flare and does not appear to have reached its quiescent level. This was obviously the case for ObsIDs 508 and 807 and very likely true for 601 and 602, so they were excluded from further analysis. Fig. 6 plots all rate data in grey (with the exception of ∼30 off-scale points associated with the largest flares), with our best estimates of the quiescent rates shown in blue.

[3] All UVOT UVW1 rates account for the ∼1 per cent per year decrease in QE reported by Breeveld et al. (2011), using mid-2009 as the baseline.
[4] http://www.swift.ac.uk/user_objects/docs.php
[5] Observations close together in time (≤4 d) were treated as single observations for this analysis: 503 + 505, 516 + 517, 518 + 519, 704 + 705, and 815 + 816. In a few observations, very short snapshots were also combined.

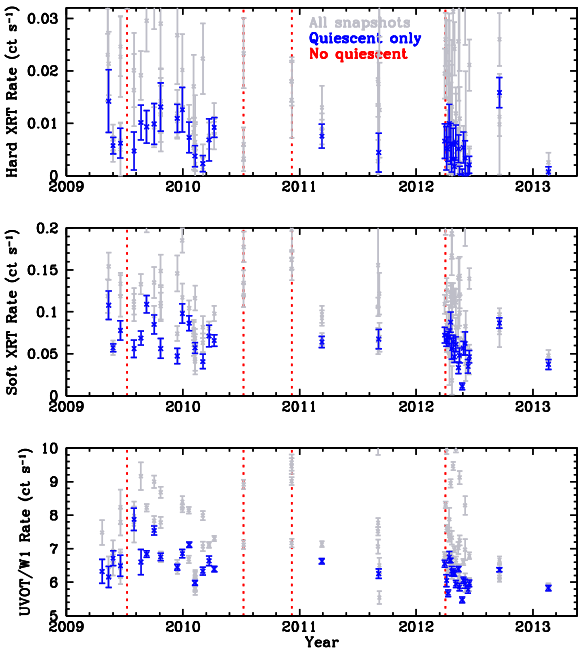

Figure 6. *Swift* XRT and UVW1 data, comparing all snapshots' event rates (grey, excluding roughly a dozen snapshots with bright flares that are off scale) with quiescent rates (blue). In four observations, marked with red vertical lines, all the snapshots were affected by flares and quiescent rates could not be determined.

Table 2. Average quiescent event rates (ct s^{-1}).

Epoch	UVW1	Soft (0.2–1.2 keV)	Hard (1.2–2.4 keV)
Cycle 5	6.597 ± 0.030	0.0662 ± 0.0023	0.00659 ± 0.00066
Cycle 8	6.137 ± 0.022	0.0483 ± 0.0018	0.00244 ± 0.00049
Diff.	0.460 ± 0.037	0.0179 ± 0.0029	0.00415 ± 0.00082
Ratio	1.075 ± 0.006	1.37 ± 0.07	2.70 ± 0.61

Note. Listed uncertainties are statistical and do not include systematic uncertainties arising from data sampling effects.

3.3.2 Evidence for X-ray periodicity

Using the *Swift* quiescent-rate data described above, we searched for periodicities using L–S periodograms. There are hints of periodicity consistent with the 7-yr photometric cycle, but without a full cycle of data the significance is low. Comparison of average quiescent rates during Cycles 5 and 8, however, provides strong evidence for variability on multiyear time-scales. As seen in Table 2, there are highly significant differences in all three energy bands (12σ for UVW1, 6σ for Soft X-ray, and 5σ for Hard X-ray), with the higher rates occurring as optical brightness nears its minimum. Relative changes in emission between high and low activities also follow the expected energy-dependent pattern (see Section 1.1), with larger changes observed at higher energies.

Fig. 7 plots the individual and Cycle-averaged *Swift* data points along with fitted sinusoids using the same period as the optical cycle but opposite in phase. Although their uncertainties are relatively large, the few points from Cycles 6 and 7 generally follow the same curves. With *Swift* data spanning only about half the optical cycle, we cannot confidently say that there is an X-ray/UV cycle, but the results are certainly consistent with and highly suggestive of such a cycle, as discussed in Section 4.

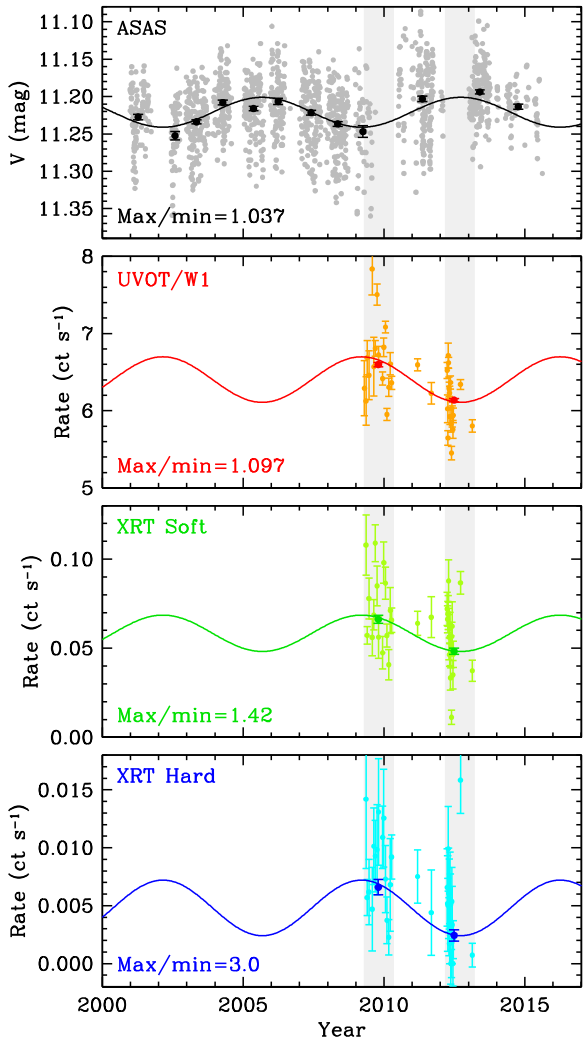

Figure 7. ASAS optical photometry and *Swift* quiescent rates. Lighter shades are used for unbinned points and darker for data averaged over year-long bins (ASAS) or *Swift* observing Cycles 5 and 8 (vertical grey bands). The UV and X-ray sinusoids were fitted using the period and (inverse) phasing from the ASAS fit.

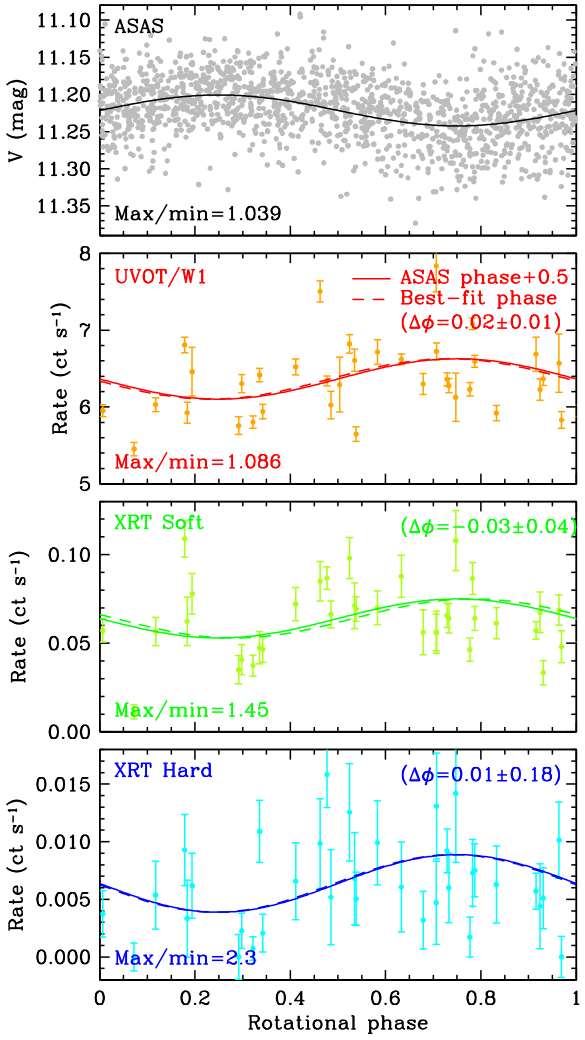

Figure 8. ASAS and *Swift* data phased to 83.1-d rotational period. The 7.05-yr fitted cycles from Fig. 7 have been subtracted from each data set. Sinusoids were fitted to *Swift* data with phases free (dashed) and fixed (solid) to that of the ASAS rotational modulation. Phase shifts ($\Delta\phi$) are relative to (inverse) ASAS phasing, i.e. $\Delta\phi = 0$ means perfect anticorrelation.

As for rotational periodicity in the *Swift* data, the L–S analysis again yields only weak evidence, usually at harmonics of the ASAS rotational period and a full or half year. We note, however, that fitting 83.1-d sinusoids to the UV and X-ray data after subtracting the 7.05-yr cycle sinusoids fitted in Fig. 7 shows that the X-ray/UV rotational modulation is ∼exactly out of phase with the *V*-band variations (see Fig. 8). We also note that the magnitudes of rotational modulation (maximum/minimum for the fitted sinusoids) in the *Swift* energy bands are very similar to those of the corresponding cyclic modulations plotted in Fig. 7, just as the ASAS optical rotational and cyclic modulations are about the same.

4 INTERPRETATION OF OPTICAL AND X-RAY/UV PERIODICITY

The simplest interpretation of the above results is that Prox Cen's X-ray, UV, and optical intensity variations are all driven by magnetic activity, with optical intensities anticorrelated with the higher energy emission. Prox Cen is therefore acting like a typical 'active' FGK star and showing a minimum of magnetic activity (and minimum X-ray/UV emission) when it is optically brightest (least spotty; e.g. Radick et al. 1998; Lockwood et al. 2007), unlike the relatively inactive Sun (see also Fig. 2). In these active stars, spots dominate the irradiance changes and associated active regions (plage) dominate the X-ray emission. (Note that spot umbrae themselves are not typically very bright in X rays; Sams, Golub & Weiss 1992).

This situation may extend to late M dwarfs as well; despite being old, Prox Cen has a relatively high L_X/L_{bol} and is therefore still 'active.' Along these lines, the relatively small photometric amplitudes seen here may actually imply more significant spot area variations. We used BT-Settl models (Allard, Homeier & Freytag 2012) to model the photometry and find reasonable results that roughly match Prox Cen's variations ($\Delta(V-I) \approx 0.18$, $\Delta V \approx 0.15$, $\Delta I \approx 0.03$; see Fig. 2) for a range of parameters. Generally, the modelled change in spot filling factor Δf_S is in the range 0.05–0.10 on top of a significant level of baseline coverage (total $f_S > 20$ per cent).

In comparison to the six stars with measured X-ray stellar cycles (see Section 1), the cycle amplitude of Prox Cen in X-rays is relatively small, with L_X^{max}/L_X^{min} roughly 1.5 versus 2–6 for the G and K

Table 3. Stellar parameters.

Star	Type	$M/M_\odot$	L_X/L_{bol}[a]	L_X^{max}/L_X^{min}	P_{cyc} (yr)	P_{rot} (d)	τ_C[b] (d)
Prox Cen	M5.5V	0.12	−4.4	1.5	7.1	83	90
61 Cyg A	K5V	0.70	−5.6[c]	2.8[c]	7.3[d]	35.4[e]	29.3
α Cen B	K1V	0.91	−6.1[f]	4.5[f]	8.1[f]	37[c]	21.2
α Cen A	G2V	1.1	−7.1[f]	∼3.4[f]	∼19[f]	28[f]	14.9
Sun	G2V	1.0	−6.7	6.3[g]	11	25.4	13.4
HD 81809	G2V	1.7	−5.9[h]	5[h]	8.2[d]	40.2[e]	20.0
ι Hor	F8V	1.25	−5.0[i]	∼1.9[i]	1.6[i]	8.2[j]	9.0

[a] L_X/L_{bol} is computed using the average of L_X^{max} and L_X^{min} over 0.2–2 keV.
[b] Convective turnover times (τ_C) are taken from Gunn, Mitrou & Doyle (1998) with extension to M dwarfs following Gilliland (1986).
[c] From Robrade et al. (2012).
[d] From Baliunas et al. (1995).
[e] From Donahue, Saar & Baliunas (1996).
[f] From Ayres (2014). Robrade et al. (2012) estimate $L_X^{max}/L_X^{min} \sim 10$ for α Cen A but the A and B components are not well resolved by *XMM–Newton* and there are also concerns regarding low-energy calibration.
[g] From Judge et al. (2003).
[h] From Favata et al. (2008), excluding the anomalous measurement likely affected by a flare.
[i] From Sanz-Forcada et al. (2013).
[j] We use an average of values ranging between 7.9 and 8.6 d found by Saar & Osten (1997), Saar et al. (1997), Metcalfe et al. (2010), and Boisse et al. (2011).

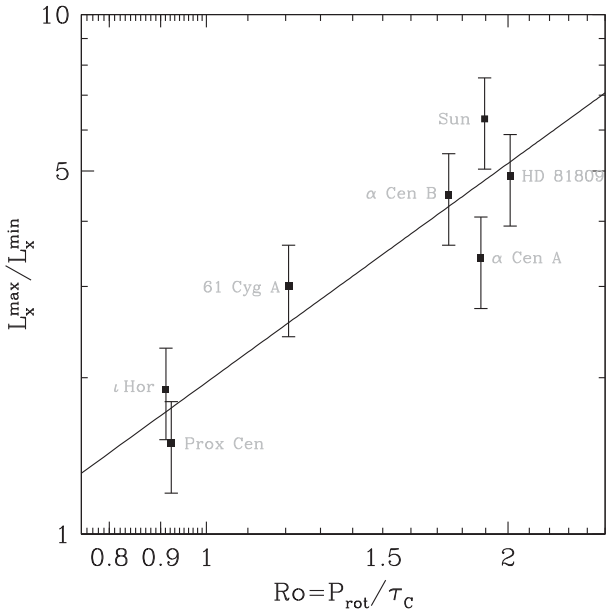

Figure 9. X-ray cycle amplitude versus Rossby number, using data from Table 3. The fitted power law is $L_X^{max}/L_X^{min} = 1.97 Ro^{1.39}$. Cycle amplitudes can vary (particularly for ι Hor) so uncertainties are not well determined; ±20 per cent error bars are shown for illustrative purposes.

stars (see Table 3). Prox Cen is, however, the most active star in this group with $\log(L_X/L_{bol}) \sim -4.4$, and there seems to be a general trend towards lower fractional quiescent variability amplitudes as activity increases.

To investigate this further, we compared various stellar parameters such as mass and rotation period and found that the best correlation was between X-ray luminosity changes and Rossby number $Ro = P_{rot}/\tau_C$, as shown in Fig. 9. The best fit using a power law yields $L_X^{max}/L_X^{min} \propto Ro^{1.4}$, which is reminiscent of the well-known rotation–activity relationship $L_X/L_{bol} \propto Ro^{-2.7}$ for partially convective stars below the saturation regime (Wright et al. 2011), which Wright & Drake (2016) showed also applies to Prox Cen and three other fully convective stars. Note that the similar characteristics of Prox Cen and ι Hor in terms of L_X^{max}/L_X^{min}, L_X/L_{bol}, and *Ro* despite their vastly different masses and rotation periods underline the importance of both rotation *and* convective time-scales, so that the 'rotation–activity' relationship is more properly thought of as the 'Rossby-number/activity' relationship.

In any case, the limited available data suggest that below the saturated regime ($L_X/L_{bol} \lesssim -3$) smaller Rossby number means higher coronal activity and lower X-ray cycle contrast, likely because more active stars are more covered with X-ray-emitting active regions even at their cycle minima, so that the contrast over a cycle is lower than for less active stars. This may be due to modulated or overlapping cycles (i.e. multiplicative or additive cycles), perhaps in combination with a steady level of underlying activity generated by, e.g. a non-cycling turbulent dynamo. Prox Cen shows no obvious signs of multiple cycles but Sanz-Forcada et al. (2013) suggest that a second longer cycle that modulates the 1.6-yr cycle might account for some of the irregular behaviour of ι Hor.

5 OTHER X-RAY OBSERVATIONS

Although *Swift*'s monitoring of Prox Cen is in some respects the most extensive of any X-ray mission to date, it covers only about half of the proposed 7-yr cycle and several other missions have comparable or greater total exposure time, often at higher event rates. As noted in Section 1.1, there are complications in comparing data from multiple instruments, and as seen in Section 3.3.1, the determination of the 'true' quiescent emission level during a given epoch may not be possible using a single observation, but thoroughness demands that we try to incorporate data from other missions in our study.

The first pointed X-ray observations (as opposed to survey scans) of Prox Cen were made by *Einstein* in 1979 and 1980 and *EXOSAT* in 1985, using proportional counters. Excluding very brief observations, the *Röntgen Satellite* (*ROSAT*) Position Sensitive Proportional Counter collected ∼36 ks of data during four observations in 1993 and early 1994. The *Rossi X-Ray Timing Explorer* made two sets of observations in 1996 February (51 ks) and 2000 May (45 ks), but its proportional counters have very little EA below 2 keV, spatial resolution is poor (1° full width at half-maximum intensity, encompassing other sources), and the background is several times as large as the quiescent signal from Prox Cen and difficult to model. See Güdel et al. (2002) and references therein for details regarding X-ray observations prior to 2002.

Given the sparse temporal coverage of these earlier missions, the limited energy resolution of proportional counters, and significant cross-calibration uncertainties, we restrict our analyses to missions with CCD detectors and list those observations in Table 4. *Chandra* data were taken from its data archive[6] while other data were downloaded from the High Energy Astrophysics Science Archive Research Center.[7] We also re-examine the *Swift* data, this time treating data from Cycle 5 collectively, and likewise for Cycle 8. The handful of observations from Cycles 6 and 7 are not included as they do not provide an adequate data sample for this analysis.

[6] http://cxc.harvard.edu/cda/
[7] http://heasarc.gsfc.nasa.gov/docs/archive.html

Table 4. Cumulative *Swift* and other X-ray observations.

Mission	Instrument	ObsID	Date	Exp. (ks)
ASCA	SIS	21022	1994 March 19	28.3
ASCA	SIS	27027	1999 August 22	57.9
Chandra	ACIS	49899+641	2000 May 7 and 9	48.9
Chandra	HETG	2388	2001 September 13	42.9
Chandra	HETG	12360	2010 December 13	79.3
XMM–Newton	PN	49350101	2001 August 12	67.4
XMM–Newton	PN	551120[3,2,4]01	2009 March 10, 12, and 14	88.8
Swift	XRT, UVW1	Cycle 5	2009 October 25[a]	38.7
Swift	XRT, UVW1	Cycle 8	2012 September 08[a]	39.5
Chandra	HRC-I	14276	2012 June 15	49.6
Chandra	HRC-I	17377	2015 December 09	35.9[b]

Notes. Exposure times are durations, without deadtime corrections.
[a]Midpoint of Prox Cen observations for that *Swift* observing Cycle.
[b]Excludes 13.8 ks when telemetry was saturated.

Including the *Swift* XRT and UVOT data, we have a total of 13 data sets from seven instruments; all but one instrument has two epochs of data. We make background-subtracted light curves for each data set with bin sizes ranging from 100 to 1000 s, depending on source and background rates. Source extraction regions are chosen to enclose ∼95 per cent of source counts and lifetime fractions are ∼99 per cent, with noted exceptions. To reduce the effect of cross-calibration uncertainties, we use a common energy range of 0.5–2.5 keV unless otherwise noted. Before explaining how the light curves were used to determine quiescent emission levels, we briefly describe the data from each instrument, proceeding in roughly chronological order. Background-subtracted light curves with corrections for enclosed energy fraction, vignetting, and livetime are shown in Fig. 10.

5.1 *ASCA*

The *Advanced Satellite for Cosmology and Astrophysics* (*ASCA*) made two observations in 1994 March and 1999 August. Measurements spanned roughly 1.5 and 2 d, respectively, but the exposures were separated into many segments of a few kiloseconds each with similar length breaks between them. We have analysed only the Solid-state Imaging Detector (SIS) data as they have better low-energy efficiency and energy resolution than the Gas Imaging Spectrometers, and have excluded a small amount of low-bit-rate data that suffer from telemetry saturation. SIS data from both detectors (SIS0 and SIS1) were collected in 1-CCD mode (except for parts of the first observation, which used 2-CCD mode) and were processed uniformly as 'Bright' mode data using standard event screening. We extracted source data from SIS0/chip1 and SIS1/chip3 using circles of radius 3 arcmin or slightly elliptical regions of the same area when the source was too close to the chip edge to fit a circle. Background was collected from a narrow ellipse of the same area along the outer edge of the chip, and the net enclosed energy fraction of the source region is ∼0.69. Pile-up is never a concern given the broad instrumental PSF.

Calibration uncertainties with this early CCD mission are large, particularly for data taken after 1994 and at low energies.[8] Examples include unphysical spectral features below 0.6 keV and a significant but uncalibrated decrease in EA below ∼1 keV over time. To reduce the impact of these issues, we extract data from 0.6 to 2.5 keV

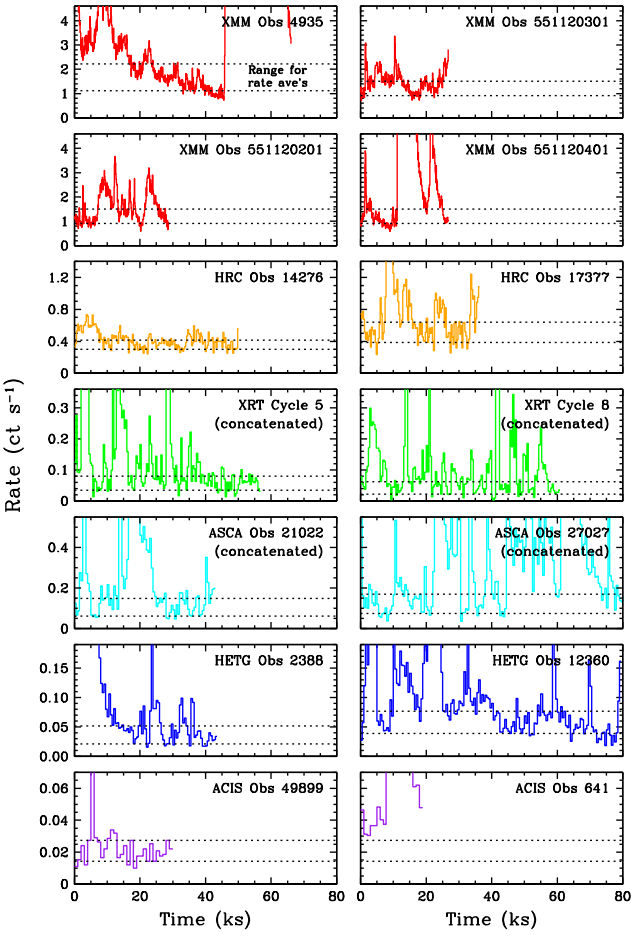

Figure 10. Light curves from X-ray missions, using data between 0.5 and 2.5 keV (0.6–2.5 keV for *ASCA*, full range for *Chandra* HRC-I). Time gaps in *Swift* XRT and *ASCA* SIS data have been removed for clarity. Horizontal dotted lines mark the 10 and 60 percentile quiescent rates shown in Fig. 11. It is likely that the first *XMM–Newton* and second HETG observations sampled little if any quiescent emission.

[8] https://heasarc.gsfc.nasa.gov/docs/asca/cal_probs.html

instead of the usual 0.5–2.5 keV, but the *ASCA* results must be viewed with skepticism.

5.2 *Chandra* ACIS

Chandra made two observations in 2000 May using ACIS-S3. The intention was to use ACIS with the LETG transmission grating but a hardware failure prevented its insertion. The core of the source was therefore heavily piled up and produced a prominent CCD readout transfer streak. We analysed these data following procedures described in Wargelin & Drake (2002), extracting unpiled data from the readout streak and annuli around the source, using regions listed in Table 1 of that work. We then created light curves (1000-s bins), subtracted background, and rescaled the net rates for each bin to recover the event rates that would have been obtained if there was no pile-up. Scaling factors ranged from 0.041 to 0.060, i.e. the measured rates were only ∼4–6 per cent of the unpiled rates. To better indicate the measured event rates, we scaled everything back down with a common factor of 0.05 before plotting in Figs 10 and 11.

5.3 *Chandra* HETG

The two HETG grating measurements were made in 2001 and 2010, both near expected cycle maxima. The event rate for 0th order is rather low so we also included ±1st orders, applying the standard spectral and background extraction regions and wavelength-dependent filtering. Pile-up reached several percent during a few flares but this does not affect our quiescent emission analysis.

5.4 *XMM–Newton*

Like the *Chandra* HETG measurements, the *XMM–Newton* observations were both made near cycle maxima. Event rates were high enough with the EPIC PN detector that we did not include data from the lower rate MOS detectors or RGS gratings. ObsID 4935 was made using PN small window mode (5.7 ms frame time) and pile-up was always negligible, although the deadtime fraction was 30 per cent. ObsID 55112 used large window mode (47.7 ms frame time) with 5 per cent deadtime and pile-up was less than 1 per cent except during large flares. The enclosed energy fraction of the 25 arcsec radius source region is 0.70.

5.5 *Swift* XRT and UVOT

The cumulative exposures for *Swift* Cycle 5 data (2009 April–2010 April) are 39 ks for the XRT and 26 ks for UVOT/UVW1, and ∼39.5 ks for both instruments during Cycle 8 (2012 March–2013 February). Pile-up was negligible except during large flares. We include UVOT data in this analysis mostly to illustrate differences in the rate distributions of UV and X-ray emission.

5.6 *Chandra* HRC-I

The HRC-I is a microchannel plate detector with practically no energy resolution but we include its two observations because they occurred three and a half years apart, near a maximum and minimum of our model 7-yr cycle; *Chandra* is an active mission and there may be more HRC-I observations for comparison in the future; the first one overlaps with a *Swift* observation (see Section 5.8). These two calibration observations were piggybacked on primary observations to measure the ACIS background while ACIS was stowed out of the telescope light path. To do this, the instrument module was moved to a location where the HRC-I could only observe Prox Cen far off the optical axis, at 15.0 arcmin for ObsID 14276 and 25.62 arcmin for ObsID 17377. This greatly broadened the source PSF, requiring large elliptical extraction regions of 155 arcsec × 102 arcsec and 354 arcsec × 216 arcsec, respectively. Roughly a quarter of the ObsID 17377 source-region counts during quiescence were from background, less for 14276.

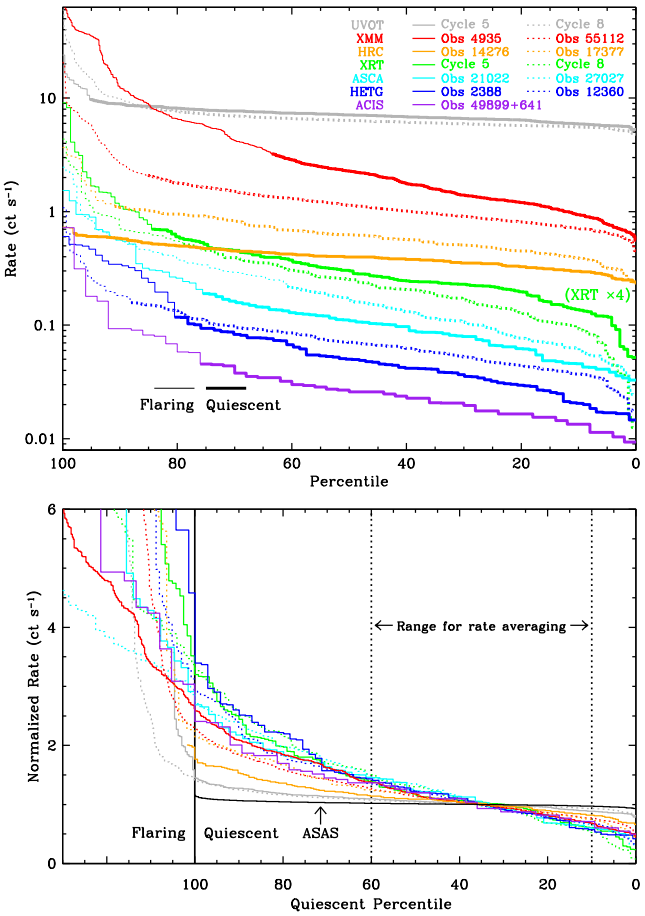

Figure 11. Light-curve rate distributions. Top: Quiescent emission is marked with thicker lines. Rates have corrections for vignetting (HRC) and deadtime (especially XMM), but ACIS data are not corrected for exclusion of the heavily piled-up PSF core. XRT rates are multiplied by four to avoid overlap with HETG data. Bottom: Quiescent data are rescaled along both axes: percentiles now refer only to quiescent emission, and each observation's rates are normalized to the average rate in the 10–60 per cent quiescent range. ASAS optical *V*-band data are plotted for comparison and are treated as if they are all quiescent. Note that instruments with less high-energy response (see Fig. 12) are less sensitive to short-term emission variability such as flares, making it easier to ascertain the longer term quiescent emission level.

During these observations, the HRC-I operated in a limited telemetry mode using only a portion of the detector. The first 13 ks and last 1 ks of the 50-ks ObsID 17377 suffered telemetry saturation caused by background 'flares.' The true source rates could not be accurately recovered during those times so they are excluded from our analysis. Telemetry was also saturated for roughly 1.5 ks in the middle of the observation because of source flaring but this does not affect our study of quiescent emission.

Event rates are corrected for vignetting, which is a significant effect so far off-axis. The correction factor is 0.753 at 15.0 arcmin

and taken from the *Chandra* calibration data base. The CALDB vignetting tables only go to 20 arcmin, but the vignetting factor for 25.62 arcmin has been previously measured and modelled to be 0.545.[9] Lastly, because the HRC-I has no useful energy resolution, the rates plotted in Fig. 11 refer to the full range of pulse heights rather than the 0.5–2.5 keV rates plotted for CCD instruments.

5.7 Determination of quiescent rates

Rate distributions with instrumental adjustments (enclosed energy fraction, livetime, vignetting) are plotted in Fig. 11. The top panel shows all the data and illustrates the large variation in event rates among different instruments, as well as the general shape of the rate distributions: relatively flat for quiescent emission, and increasingly steep and unpredictable for higher rate, less frequent flares. Our interest here is on the flattest part of the distributions, where rates are relatively insensitive to the choice of sampling range.

Deciding where to draw the line between flaring and quiescent emission is somewhat subjective, but normalizing the distributions along both axes as shown in the bottom panel is helpful in guiding that judgment. We iteratively adjusted the flare/quiet break for each curve in the top panel and plotted the results in the bottom panel, aiming to have the curves overlap as much as possible, placing the highest emphasis on the degree of overlap in the nearly linear 10–60 per cent quiescent range marked with dotted lines (used to calculate our quiescent reference rates) and least emphasis in the inherently more variable flaring range.

We were unable to craft an automated method of doing this but believe our results are reasonably objective. We exclude the lowest 10 per cent from our calculations because of that range's non-linear rate distributions, which may be caused in part by statistical artefacts from low-count binning, outlier source fluctuations, or instrumental/processing defects (particularly for the XRT with its damaged CCD pixels). The upper limit of 60 per cent aims to maximize the sampling basis while minimizing flare contamination. Changing the flare/quiet break by ±10 per cent (using percentiles in the top panel of Fig. 11) changes the reference quiescent rates for X-ray instruments by typically 6 per cent, ranging from 10 per cent for *ASCA* ObsID 27027 to 2 per cent for HRC-I ObsID 14276. The corresponding UVW1 sensitivity is ∼1.3 per cent, and the even flatter ASAS-3 distribution is shown for comparison.

The sensitivity of inferred quiescent rates to the location of the flare/quiet break is effectively given by the slope of the rate distributions in the quiescent range (easiest to compare in the ∼50–100 per cent range of the bottom panel of Fig. 11), e.g. the HRC-I distributions are the flattest of the X-ray data, followed by *XMM–Newton* and ACIS on up to the steepest distributions of *ASCA* and the HETG. This is in turn highly correlated with the various instruments' energy-dependent EAs as shown in Fig. 12. Again using the HETG as an example, its rate distributions have steep slopes while its EA is weighted heavily towards the higher energies typical of emission from hot plasma, which shows more intensity variation than emission at lower energies. At the other extreme, the HRC-I rate distributions are the flattest while the HRC EA is more heavily weighted towards low energies where emission is less variable. All things otherwise being the same, we would therefore expect HRC observations to be the most likely to yield accurate quiescent-rate measurements while instruments with higher proportions of high-energy EA, being more sensitive to high-T flare emission, are less likely to observed periods when high-T (non-quiescent) emission is minor.

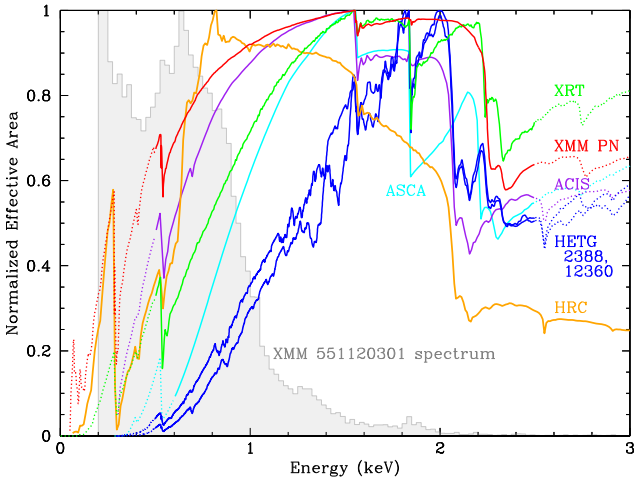

Figure 12. Normalized X-ray instrument EAs, illustrating differences in energy dependence. Solid lines show the 0.5–2.5 keV energy range used for rate measurements (0.6–2.5 keV for *ASCA*); the HRC-I has no energy resolution so its full range was used. An *XMM–Newton* spectrum is shown to illustrate that most emission occurs at relatively low energies. Instruments with more area at higher energies, such as the HETG, detect relatively more high energy (more variable) emission.

One weakness of the rate distribution analysis is that temporal information is ignored. One can see in Fig. 10 that the first two-thirds of *XMM–Newton* ObsID 4935 very likely includes the slow decay of a large flare and so this observation probably never sampled quiescent emission. HETG ObsID 12360 exhibits a less-obvious decline but our estimated quiescent rate is again probably too high. The quiescent rate in *ASCA* ObsID 27027 may also be overestimated.

5.8 Rate to luminosity conversions

With this analysis method, we obtain UVW1 rates for *Swift* Cycles 5 and 8 of 6.618 and 6.061 ct s^{-1} (a difference of 9.2 per cent) versus rates of 6.597 and 6.137 (difference of 7.5 per cent) obtained using the 'quiescent snapshot' method (see Table 2), which is good agreement given the various sources of uncertainty in both approaches.

To compare emission observed by the many X-ray instruments, we must convert their average quiescent event rates to 0.5–2.5 keV luminosities, which we did using the Portable Interactive Multi-Mission Simulator (PIMMS; v. 4.8) tool.[10] As noted before, instrument responses can vary a great deal as a function of energy (see Fig. 12) and, to a lesser degree, time (for *Chandra* and *ASCA*). PIMMS-derived luminosities are plotted in Fig. 13, showing that results for some instruments, particularly the HRC-I and HETG, strongly depend on the assumed temperature. For consistency, and because some spectra did not have enough counts to permit detailed modelling, we used a single set of plasma parameters for all the PIMMS rate conversions. Those values were derived from fits to *XMM–Newton* spectra, which had by far the most counts. Auxiliary Response Functions and Response Matrix Functions were created for ObsIDs 4935 and 55112 using the Scientific Analysis System v. 1.2 (SAS)[11]

[9] http://cxc.harvard.edu/ccr/proceedings/02_proc/presentations/bradw/rxj/

[10] https://heasarc.gsfc.nasa.gov/docs/software/tools/pimms.html

[11] http://www.cosmos.esa.int/web/xmm-newton/sas

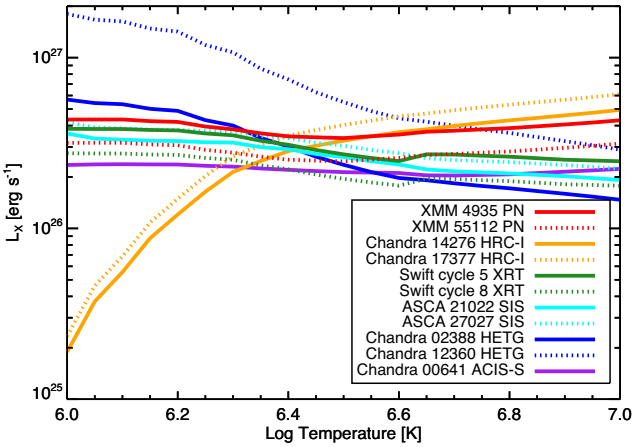

Figure 13. X-ray luminosities as a function of T, derived from measured quiescent reference rates via PIMMS.

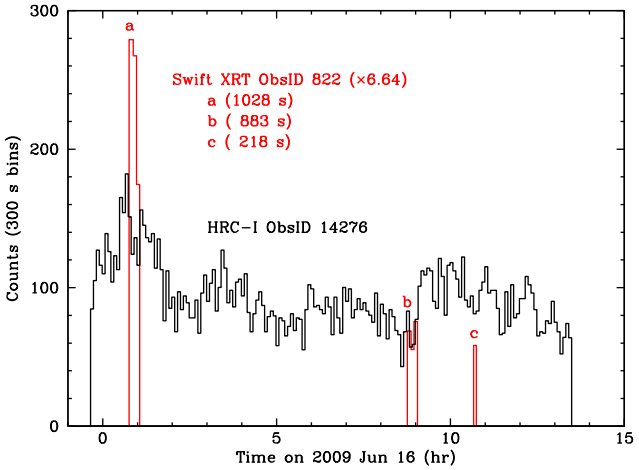

Figure 14. Background-subtracted light curves of overlapping *Swift* XRT and *Chandra* HRC observations. *Swift* snapshots were each evenly divided into an integer number of bins and their counts (0.5–2.5 keV) rescaled for 300-s bins. Events during *Swift* snapshots 822b and 822c were used to cross-calibrate the two instruments. The rate difference during snapshot 822a is because the XRT's CCD detector is more sensitive than the HRC to the higher energy emission from hotter (flaring) plasma (see Fig. 12).

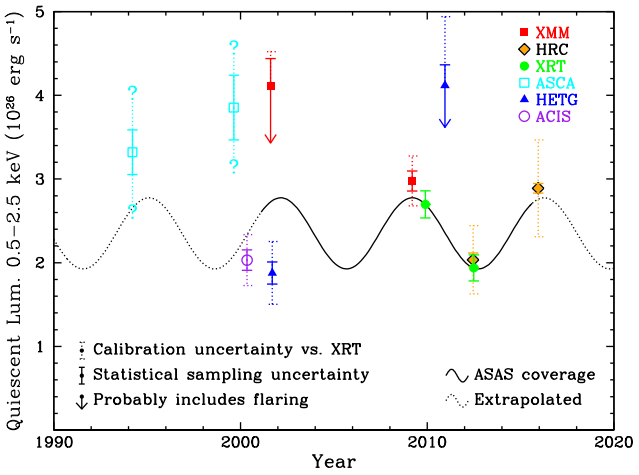

Figure 15. Quiescent X-ray luminosities (0.5–2.5 keV) over time, with the optical 7.05-yr cycle scaled to match XRT data. See text and Table 5 for details regarding error bars.

`evselect` command, with standard `flag=0` and `pattern=0:4` (sd) event filtering.

To fit the spectra, we used the Sherpa modelling and fitting package (Freeman, Doe & Siemiginowska 2001) with a two-temperature APEC coronal emission model. Column density was set to 10^{18} cm^2, providing negligible absorption. The best fit to the ObsID 5512 quiescent spectrum was obtained using 70 per cent $kT_1 = 0.23$ keV, 30 per cent $kT_2 = 0.80$ keV, and 0.25 solar abundance. Results for ObsID 4935 were similar but with higher flux. Because of previously noted concerns over whether that observation includes truly quiescent emission used the ObsID 55112 results in all our PIMMS calculations.

Even with what should be well-determined plasma parameters, the sensitivity of the HRC-I rate-to-luminosity calculations to the assumed temperature is a concern, especially in light of the challenges faced by Ayres (2009) when comparing measurements from different instruments (see Section 1.1). Luckily, one of the *Swift* observations overlaps with the first HRC observation, as seen in Fig. 14. Two of the three ObsID 822 snapshots collected quiescent emission, allowing a direct cross-calibration of HRC and XRT rates. During the time of overlap, the HRC collected 333 events (with estimated 95 background) versus 39 (3 background) for the XRT in the 0.5–2.5 keV range, yielding a ratio of 6.64 ± 1.33. Fig. 14 also nicely illustrates that the HRC is significantly less sensitive to emission from flares than the *Swift* XRT and other instruments that have more of their EA at higher energies than the HRC (see Fig. 12). Note that using the PIMMS-derived HRC-I curves in Fig. 13 would yield luminosities roughly twice the values we compute from cross-calibration with the XRT; we have no obvious explanation, but again point to the difficulties of reconciling results from instruments with different energy responses.

5.9 Results and uncertainties

The resulting quiescent X-ray luminosities measured over the past 22 yr are shown in Fig. 15, with the optical 7-yr cycle scaled to intercept the two *Swift* XRT points. Error bars reflect information in Table 5. For each point, solid error bars denote 'statistical sampling' uncertainties arising from the choice of the flare/quiet break in Fig. 11 (see Section 5.7). Dotted error bars are estimated uncertainties from cross-calibration with the *Swift* XRT. Based on work by the International Astronomical Consortium for High Energy Calibration (e.g. Tsujimoto et al. 2011; Plucinsky et al. 2016), these latter errors are typically ∼10 per cent at energies greater than about 0.9 keV (15–20 per cent around 0.6 keV) for missions launched after the mid-1990s, but the relatively high sensitivity of the *Chandra* HETG observations to temperature uncertainties and the special treatment required for the piled-up ACIS observations lead us to increase uncertainties for these instruments.

As noted earlier, *ASCA*'s calibration uncertainties are rather large at low energies and increased over time. We include its measurements in Fig. 15 but they should be given little weight. HRC-I luminosities are even more sensitive to T uncertainties than the HETG, but our direct calibration versus the XRT is accurate to 20 per cent. Relative calibration uncertainty between the two HRC-I observations is tiny because the EA is very nearly constant, and Prox Cen's quiescent luminosity during ObsID 17377 (2015 December) is clearly higher than during ObsID 14276 (2012 September).

Subjective sampling errors are assigned based on judgements of the likelihood that our quiescent rates may be incorrect (generally

Table 5. Luminosity uncertainties.

Observation	Calibration error versus XRT (%)	Statistical sampling error (%)	Subjective sampling error
ASCA 21022	?	8	Low
ASCA 27027	?	10	Medium
ACIS 49899+641	15	6	Low
HETG 2388	20	7	Low
HETG 12360	20	6	High
XMM–Newton 4935	10	8	Very high
XMM–Newton 55112	10	4	Low
Swift XRT Cycle 5	–	6	Very low
Swift XRT Cycle 8	–	8	Very low
HRC-I 14276	20	4	Low
HRC-I 17377	20	2	Low

Note. Statistical sampling error is the change in the calculated quiescent rate when the flare/quiet break in Fig. 11 changes by 10 per cent. Subjective sampling error reflects the likelihood that the presumed quiescent emission includes significant contamination from flares.

meaning too high because of the inclusion of flare emission). Measurements are most reliable when they come from long, multiple observations over a period of time. In both cases, the key advantage is a higher probability of observing emission during periods of quiescence. Multiple observations, such as *Swift*'s, that span periods comparable to or longer than Prox Cen's 83-d rotation period have the additional advantage of sampling emission over more of the stellar surface. In practice, given Prox Cen's propensity for flaring and the spatial nonuniformity that gives rise to its rotational intensity modulation, there will always be some ambiguity in what constitutes 'quiescent' emission, but the *Swift* observations should provide the best measurements and we assign them a 'very low' sampling error in Table 5.

At the other extreme, as noted at the end of Section 5.7, *XMM–Newton* ObsID 4935 probably had significant flare contamination during its entire exposure, and our quiescent rates estimates for HETG ObsID 12360 are also likely to be too high. Both of these measurements are marked in Fig. 15 with upper limits.

For these reasons we assign the most significance to the *Swift* XRT data, followed by the HRC measurements, all of which are in good (anticorrelated) accord with the 7-yr optical cycle as are the *Swift* UVOT/UVW1 measurements. Observations by other X-ray missions are, after considering the likelihood of flare contamination in some measurements, also consistent with a cycle, although given the estimated uncertainties one cannot draw too many conclusions. There are also uncertainties from extrapolation of the optical cycle to times before the first ASAS data in late 2000; as illustrated particularly well by the Sun's most recent cycles, there can be significant differences in period and amplitude from one cycle to the next.

6 SUMMARY

We have presented an analysis of 15 yr of ASAS *V*-band optical monitoring data on Proxima Cen, finding strong evidence for periodic 7-yr variations and confirming previous measurements of an 83-d rotation period by Benedict et al. (1998), Kiraga & Stepień (2007), Savanov (2012), and Suárez Mascareño et al. (2016). We do not see any evidence for the 1.2- or 3-yr periodicities tentatively reported by Cincunegui et al. (2007) or Benedict et al. (1998), respectively, but our 7.05-yr optical period is in accord with the intriguing peak around 7 yr noted by Endl & Kürster (2008) in their analysis of radial velocity data and with 6.8 ± 0.3 yr derived by Suárez Mascareño et al. (2016) from a smaller set of ASAS data.

The amplitude of *V*-band rotational modulation was observed to vary significantly on few-year time-scales but the phase of the variations was remarkably consistent. The lack of *I*-band variation combined with a strong trend in $V - I$ versus V, with the star growing redder when fainter, implies that Prox Cen likely has a significant filling factor of cool starspots. ASAS *V*-band data show evidence for DR, in the form of distinct $P_{\rm rot}$ values in different epochs. The fractional DR rate is $\Delta P_{\rm rot}/\langle P_{\rm rot}\rangle \sim 0.16$, similar to the solar value and broadly consistent with observed trends in single dwarfs (Saar 2011).

Our analysis of 4 yr of *Swift* data (2009–2013) strengthens the case for a stellar cycle by extending it to higher energies, with observed peak-to-peak variations of order 10 per cent in the UVW1 band and roughly a factor of 1.5 in the 0.5–2 keV X-ray band, with X-ray/UV variations anticorrelated with optical brightness. This anticorrelation is also seen (with less confidence) in rotational modulation, as would be expected if higher starspot coverage (which generates more X-ray/UV emission) causes a net decrease in optical emission. Comparing against six other stars with measured X-ray cycles, we find that cycle amplitude correlates with Rossby number according to $L_{\rm X}^{\rm max}/L_{\rm X}^{\rm min} \propto Ro^{1.39}$, indicating that the X-ray cycle amplitude decreases with increasing coronal activity, consistent with the idea that higher activity stars have a greater fraction of their surfaces covered by active regions and therefore less potential to increase X-ray emission at cycle maxima.

Two recent *Chandra* HRC-I observations, one of which occurred during a *Swift* observation allowing accurate cross-calibration, extend X-ray coverage to late 2015 and are in excellent agreement with the presumed cycle, as is the most recent *XMM–Newton* measurement in 2009. Our most reliable measurements therefore now cover two cycle maxima and one minimum. Other data from previous and currently operating X-ray missions extending back more than two decades yield more ambiguous results, illustrating the difficulty of measuring quiescent emission in active stars such as Prox Cen when observations are few and infrequent. Complications when comparing results from different instruments were also highlighted.

The apparent 7-yr stellar cycle in Prox Cen, a fully convective M5.5 star, is in conflict with most models of magnetic dynamo theory and should spur further theoretical work in this area. Further evidence that dynamo behaviour in fully convective stars does not follow canonical theory is provided by Wright & Drake (2016), who found that the X-ray emission of four fully convective stars, including Prox Cen, correlates with Rossby number in the same way as in solar-type stars. The X-ray activity–rotation relationship has long been established as a proxy for magnetic dynamo action; these results, combined with our finding of Proxima's stellar cycle, therefore suggest that fully convective stars operate dynamos similar to that of the Sun, with the implication that a radiative core and its tachocline are not critical or necessary ingredients.

Our study of 15 yr and 1085 nights of ASAS *V*-band optical photometry, 3 yr of *I*-band observations, 4 yr and 125 *Swift* X-ray and UV exposures, and two decades of observations by other X-ray missions comprises by far the most extensive analysis of long-term monitoring data on an M dwarf and also provides the best evidence for a stellar cycle in an isolated fully convective star. The ASAS-4 monitoring program is continuing to collect data and the All-Sky Automated Survey for Supernovae (Shappee et al. 2014) obtained its first observation of the field containing Prox Cen on 2016 March 9 (B. Shappee, private communication), so

there are excellent prospects for sustained optical monitoring of this star.

Additional X-ray data would be even more valuable but are harder to obtain than optical data, and determinations of quiescent luminosities are a challenge because of frequent flaring. Our work shows that reliable measurements of quiescent emission can be made even when monitoring active stars such as Prox Cen, but that this is most easily accomplished when there are several observations per year that sample all sides of the star, made by the same instrument (or multiple instruments with good cross-calibration), and preferably in softer energy ranges less sensitive to flares. Each observation can be quite short, however, so that with the proper instrument(s) a modest investment of observing time can yield UV and X-ray data vital for the study of cyclic and other medium- to long-term stellar behaviour.

ACKNOWLEDGEMENTS

This work was supported by NASA's *Swift* Guest Investigator program under Grants NNX09AR09G and NNX13AC61G. BJW, JJD, and VLK were also supported by NASA contract NAS8-39073 to the *Chandra* X-Ray Center, and SHS was supported by NASA Heliophysics grant NNX16AB79G. We thank the *Swift* team and especially the PI, Neil Gehrels, for providing TOO/Discretionary time, without which much of this work would have been impossible. We also thank Ben Shappee for helpful conversations and the ASAS collaboration for providing optical photometry data. This work made use of data supplied by the UK *Swift* Science Data Centre at the University of Leicester, and data and software provided by the High Energy Astrophysics Science Archive Research Center (HEASARC), which is a service of the Astrophysics Science Division at NASA/GSFC and the High Energy Astrophysics Division of the Smithsonian Astrophysical Observatory.

REFERENCES

Alekseev I. Y., 2005, Astrophysics, 48, 20
Allard F., Homeier D., Freytag B., 2012, Phil. Trans. R. Soc. A, 370, 2765
Anglada-Escudé G. et al., 2016, Nature, 536, 437
Aschwanden M. J., 1994, Solar Phys., 152, 53
Ayres T. R., 2009, ApJ, 696, 1931
Ayres T. R., 2014, AJ, 147, 59
Ayres T. R., Judge P. G., Saar S. H., Schmitt J. H. M. M., 2008, ApJ, 678, L121
Baliunas S. L. et al., 1995, ApJ, 438, 269
Benedict G. F. et al., 1993, PASP, 105, 487
Benedict G. F. et al., 1998, ApJ, 116, 429
Berdyugina S. V., 2007, Mem. Soc. Astron. Ital., 78, 242
Bessell M. S., 1991, AJ, 101, 662
Boisse1 I., Bouchy F., Hébrard G., Bonfils X., Santos N., Vauclair S., 2011, A&A, 528, A4
Breeveld A., Landsman W., Holland S. T., Roming P., Kuin N. P. M., Page M. J., 2011, in McEnery J. E., Racusin J. L., Gehrels N., eds, AIP Conf. Proc. Vol. 1358, Gamma Ray Bursts 2010. Am. Inst. Phys., New York, p. 373
Brown B. P., Browning M. K., Brun A. S., Miesch M. S., Toomre J., 2011a, ApJ, 711, 424
Brown B. P., Miesch M. S., Browning M. K., Brun A. S., Toomre J., 2011b, ApJ, 731, 69
Buccino A. P., Mauas P. J. D., 2008, A&A, 483, 903
Buccino A. P., Petrucci R., Jofré E., Mauas P. J. D., 2014, ApJ, 781, L9
Burrows D. N. et al., 2005, Space Sci. Rev., 120, 165
Chabrier G., Baraffe I., 1997, A&A, 327, 1039
Chabrier G., Küker M., 2006, A&A, 446, 1027
Cincunegui C., Mauas P. J. D., 2004, A&A, 414, 699
Cincunegui C., Díaz R. F., Mauas P. J. D., 2007, A&A, 461, 1107
Cochran W. D., Hatzes A. P., 1993, in Phillips J. A., Thorsett S. E., Kulkarni S. R., eds, ASP Conf. Ser. Vol. 36, Planets Around Pulsars. Astron. Soc. Pac., San Francisco, p. 267
Cohen O., Ma Y., Drake J. J., Glocer A., Garraffo C., Bell J. M., Gombosi T. I., 2015, ApJ, 806, 41
DeWarf L. E., Datin K. M., Guinan E. F., 2010, ApJ, 722, 343
Díaz R. F., González J. F., Cincunegui C., Mauas P. J. D., 2007, A&A, 474, 345
Dikpati M., Charbonneau P., 1999, ApJ, 518, 508
Donahue R. A., Saar S. H., Baliunas S. L., 1996, ApJ, 466, 384
Drake J. J., Ratzlaff P., Kashyap V., Huenemoerder D. P., Wargelin B. J., Pease D. O., 2014, ApJ, 783, 2
Endl M., Kürster M., 2008 A&A, 488, 1149
Endl M., Cochran W. D., Tull R. R., MacQueen P., 2003, AJ, 126, 3099
Evans P. A. et al., 2009, MNRAS, 397, 1177
Favata F., Micela G., Orlando S., Schmitt J. H. M. M., Sciortino S., Hall J., 2008, A&A, 490, 1121
Freeman P., Doe S., Siemiginowska A., 2001, in Starck J.-L., Murtagh F. D., eds, Proc. SPIE Conf. Ser. Vol. 4477, Astronomical Data Analysis. SPIE, Bellingham, p. 76
Gastine T., Duarte L., Wicht J., 2012, A&A, 546, A19
Gilliland R. L., 1986, ApJ, 300, 339
Gomes da Silva J., Santos N. C., Bonfils X., Delfosse X., Forveille T., Udry S., 2011, A&A, 534, A30
Gomes da Silva J., Santos N. C., Bonfils X., Delfosse X., Forveille T., Udry S., Dumusque X., Lovis C., 2012, A&A, 541, A9
Güdel M., Audard M., Skinner S. L., Horvath M. I., 2002, ApJ, 580, L73
Guinan E. F., 2010, Chandra AO12 proposal abstract 12200639
Guinan E. F., Morgan N. D., 1996, BAAS, 28, 942
Gunn A. G., Mitrou C. K., Doyle J. G., 1998, MNRAS, 296, 150
Hempelmann A., Robrade J., Schmitt J. H. M. M., Favata F., Baliunas S. L., Hall J. C., 2006, A&A, 460, 261
Henry T. J., Kirkpatrick J. D., Simons D. A., 1994, AJ, 108, 1437
Hoffman J., Günther H. M., Wright N. J., 2012 ApJ, 759, 145
Horne J. H., Baliunas S. L., 1986, ApJ, 302, 757
Hosey A. D., Henry T. J., Jao W.-C., Dieterich S. B., Winters J. G., Lurie J. C., Riedel A. R., Subasavage J. P., 2015, AJ, 150, 6
Jao W.-C., Henry T. J., Subasavage J. P., Winters J. G., Gies D. R., Riedel A. R., Ianna P. A., 2014, AJ, 147, 21
Jason M., Guinan E., Engle S., Pojmański G., 2007, BAAS, 39, 921
Jay J. E., Guinan E. F., Morgan N. D., Messina S., Jassour D., 1997, BAAS, 29, 730
Judge P. G., Solomon S. C., Ayres T. R., 2003, ApJ, 593, 534
Käpylä P. J., Mantere M. J., Brandenburg A., 2013, Geophys. Astrophys. Fluid Dyn., 107, 244
Khodachenko M. L. et al., 2007, Astrobiology, 7, 167
Kiraga M., Stepień K., 2007, Acta Astron., 57, 149
Kuin N. P. M. et al., 2015, MNRAS, 449, 2514
Lammer H., Selsis F., Ribas I., Guinan E. F., Bauer S. J., Weiss W. W., 2003, ApJ, 598, L121
Lehtinen J., Jetsu L., Hackman T., Kajatkari P., Henry G. W., 2016, A&A, 588, A38
Lockwood G. W., Skiff B. A., Henry G. W., Henry S., Radick R. R., Baliunas S. L., Donahue R. A., Soon W., 2007, ApJS, 171, 260
Lurie J. C. et al., 2014, AJ, 148, 91
Mayor M. et al., 2003, The Messenger, 114, 20
Metcalfe T. S., Basu S., Henry T. J., Soderblom D. R., Judge P. G., Knölker M., Mathur S., Rempel M., 2010 ApJ, 723, L213
Mullan D. J., MacDonald J., 2001, ApJ, 559, 353
Owen J. E., Mohanty S., 2016, MNRAS, 459, 4088
Penz T., Micela G., 2008, A&A, 479, 579
Plucinsky P. P., Beardmore A. P., Foster A., Haberl F., Pollock A. M. T., Sembay S., 2016, A&A, in press
Pojmański G., 1997, Acta Astron., 47, 467
Pojmański G., 2002, Acta Astron., 52, 397
Queloz D. et al., 2001, A&A, 379, 279

Radick R. R., Lockwood G. W., Skiff B. A., Baliunas S. L., 1998, ApJS, 118, 239
Reiners A., Basri G., 2008 A&A, 489, L45
Robertson P., Endl M., Cochran W. D., Dodson-Robinson S. E., 2013, ApJ, 764, 3
Robrade J., Schmitt J. H. M. M., Favata F., 2012, A&A, 543, A84
Roming W. A. et al., 2005, Space Sci. Rev., 120, 95
Rüdiger G., Elstner D., Ossendrijver M., 2003, A&A, 406, 15
Saar S. H., 2011, in Debi C., Klaus S., eds, Proc. IAU Symp. 273, The Physics of Sun and Star Spots. Cambridge Univ. Press, Cambridge, p. 61
Saar S. H., Osten R. A., 1997, MNRAS, 284, 803
Saar S. H., Huovelin R. A., Osten R. A., Shcherbakov A. G., 1997, A&A, 326, 741
Sams B. J., III, Golub L., Weiss N. O., 1992, ApJ, 399, 313
Sanz-Forcada J., Stelzer B., Metcalfe T. S., 2013, A&A, 553, L6
Savanov I. S., 2012, Astron. Rep., 56, 716
Scargle J. D., 1982, ApJ, 263, 835
Shappee B. J. et al., 2014, ApJ, 788, 48
Suárez Mascareño A., Rebolo R., González Hernández J. I., 2016, A&A, 595, A12
Tsujimoto M. et al., 2011, A&A, 525, A25
Vida K., Kriskovics L., Oláh K., 2013, Astron. Nachr., 9, 972
Wagner W. J., 1988, Adv. Space Res., 8, 67
Wargelin B. J., Drake J. J., 2002, ApJ, 578, 503
Wilson O. C., 1978, ApJ, 226, 379
Wright N. J., Drake J. J., 2016, Nature, 535, 526
Wright N. J., Drake J. J., Mamajek E. E., Henry G. W., 2011, ApJ, 743, 48

This paper has been typeset from a TEX/LATEX file prepared by the author.